Influence of HAZ microstructure on RCF under twin-disc test of a flash-butt welded rail

Henrique Boschetti Pereira, Universidade de São Paulo

Edwan Anderson Ariza Echeverri, Universidad del Magdalena

Luiz Henrique Dias Alves, Universidade Federal de Juiz de Fora

Kazim Yildirimli, The University of Sheffield

Roger Lewis, The University of Sheffield

Hélio Goldenstein, Universidade de São Paulo

Abstract

A new twin-disc test was performed employing discs that incorporate all microstructure regions within the heat-affected zone (HAZ) of flash-butt welded rails. It was observed that the lower hardness regions (spheroidized cementite in a ferritic matrix) at the HAZ boundary underwent a local deformation, generating valleys and reproducing a common defect type observed in rail welds: double squat-like defect. Longer crack lengths or crack clusters were observed in the HAZ boundary and central weld regions. The cross-section metallography showed that these cracks are directly related to the microstructure of spheroidized cementite at the HAZ edges or pro-eutectoid ferrite at the central region. The decrease in surface roughness before the cracks, the presence of oxide on the bottom crack surface, and superior spheroidized cementite microstructure in the upper crack region suggest that these larger/cluster cracks are predominated by extrusion of the softer material above the harder material (pearlitic/base metal).

Key-words: Steel; Heat-Affected Zone; Flash-butt Weld; Rail; Twin-disc test; Squat-like defect.

Symbol:

RCF - Rolling contact fatigue

BHN - Brinell Hardness Number

HAZ - Heat-affected zone

DET - Divorced eutectoid transformation

SUROS - University of Sheffield Rolling Sliding rig

SEM - scanning electron microscopy

COT - Coefficient of Traction

HL - hardness-loss

SL - specimen location

WEL - White etching layer

1. Introduction

Component surface degradation can occur through two main mechanisms - wear and RCF. Wear involves the gradual loss of material due to friction and contact with other surfaces. RCF, on the other hand, consists of the formation of surface cracks due to repeated contact stresses. These mechanisms are interconnected, as wear can increase the likelihood of RCF by altering the surface properties and thus causing stress concentrations. At the same time, RCF can accelerate wear by creating rough surfaces and removing material.

Railroad history and rolling contact fatigue are intrinsically connected due to the wheel and rail contact interaction. In the 1960s, the steel rails featured a hypo-eutectoid chemical composition, marked by a microstructure comprising pro-eutectoid ferrite with pearlite, with wear and Rolling Contact Fatigue (RCF) identified as the primary failure modes. With the development of new rail steels, compositions adhering to the chemical eutectoid balance, yielding a fully pearlitic microstructure, have been formulated, enhancing resistance to rolling contact fatigue. Still, the main failure mode continued to be the wear. Contemporary steels generally have a hyper-eutectoid composition, but with accelerated cooling heat treatment, the microstructure is composed only of fine pearlite. These steels have increased the hardness considerably, although the main failure mode now is by RCF [1].

During contact between wheel and rail, there is an interaction between mechanical and interface forces. Different forms of damage compete with each other, these being wear and crack formation, mainly RCF [2]. Wear can be divided into at least three modes: mild, severe, and catastrophic, and can be characterized according to wear rate, wear surface topography, and debris characteristics. The transition from these modes depends on environmental, sliding, and loading conditions [3]. Thus, wear is proportional to the amount of energy and a fraction of the dissipated energy of a system and is also composed of sound and temperature [3,4]. Wear competes with other mechanisms generated by wheel-rail interaction, such as RCF, and an optimum wear rate causes the material to lose surface mass faster than RCF crack formation. This optimum wear rate serves as a grinding process for the rail, preventing crack propagation before its further propagation [5,6].

In modern railroads, the rails are welded; their hypereutectoid composition and extreme microstructure refinement, with an interlamellar spacing of less than 0.1 µm and hardness above 400 BHN, present new difficulties. The welding process is partly done in welding yards (flash-butt weld process) and partly in the field, usually an aluminothermic process. The welding process significantly changes the material's microstructure locally,

3

especially in heat-affected areas. Mansouri and Monshi [7], Porcaro *et al.* [8,9], Bauri *et al.* [10,11], among others, have identified different regions along the heat-affected zone (HAZ) of rails flash-butt welding, and are illustrated in Figure 1. This microstructural change results in the formation of spheroidized pearlite, softening this region[7,8]. The extent and intensity of this change is a significant problem for rail maintenance management, making maintenance prediction work difficult and operation unreliable, with increased fracture risk [12–14].
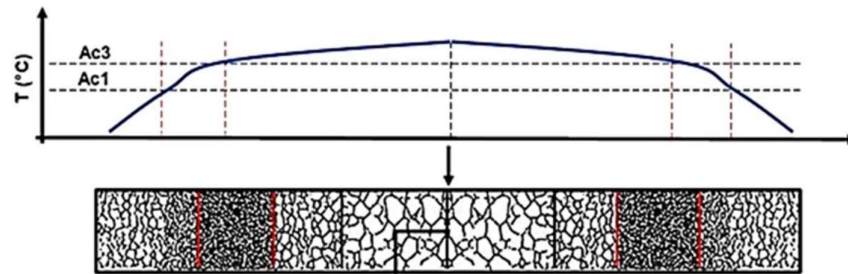

Figure 1 – Schematic representation of the relationship between microstructure and temperature distribution in the flash-butt welding process. The centre line consists of pro-eutectoid ferrite, followed by a region of increasing austenitic grains, a region of austenitic grain refinement, and an area of partial austenitization resulting in cementite spheroidization (adapted from [7,11]).

Manufacturing continuous rail without connectors has increased the integrity of the material during use. Thermite welding (aluminothermic) or flash-butt welding can be used to make continuous rails. Continuous rails have no interface between rail sections and can be kilometres in length. The benefit of this type of rail is the absence of wheel impact between each junction, reducing maintenance in general [15,16].

Generally, the flash-butt welding is performed in fixed construction sites, but mobile flash-butt welding is becoming more common [17,18]. Mobile welding is performed in the field with a unit to transport the equipment, possibly by truck or train. The equipment has an electricity transformer that allows the welding.

Mobile flash-butt welding has lower heat input, consequently making welding high carbon and alloying elements rails very challenging, such as Premium and Super Premium rails. The higher amount of Ce (carbon equivalent) increases the material's strength of the material, making it more difficult to weld [10,19,20]. Furthermore, narrow HAZ size flash-butt welding can favour the formation of brittle phases such as martensite [21] and significantly increase the residual stress [22].

Some research has conducted experiments to optimize flash-butt welding parameters [10,20]. Tensile tests showed double necking, which occurred in the

spheroidization region. Different behaviour was observed depending on the microstructure of the HAZ. In some cases, the fracture took place outside the necking due to grain boundaries cementite precipitation [10].

The microstructural heterogeneity of the HAZ of welded rails has some peculiar characteristics. In the central region, pro-eutectoid ferrite formation may occur due to decarburization during the flashing process [10]. In the adjacent areas, a large grain size region, refined grain size, and spheroidization region significantly decrease the hardness locally [7,9]. The spheroidization region is formed by the divorced eutectoid transformation (DET) [23] due to partial austenitization, leaving cementite as a pre-nuclei for spheroidization during the cooling step [24–26].

Several studies on the influence of microstructure on rolling contact fatigue (RCF) have been performed, aiming for the optimization between bainite and pearlite [27–29]. Although, twin-disc tests were performed with different microstructures obtained by heat treatments that simulated the extreme conditions of a HAZ from a rail weld: fully pearlitic and spheroidized cementite (DET). The results showed that the test pair of pearlite with DET (softer disc) increased the surface hardness of the DET disc to a greater magnitude than the pearlitic disc, initially inducing cracking in the harder starting material [30]. A better understanding of the nucleation and propagation process can improve the knowledge in monitoring contact fatigue crack nucleation and propagation process. The next step of this research will be to obtain discs from actual welds and perform twin-disc RCF tests.

The greatest difficulty in performing twin disc testing is microstructural heterogeneity. As there are regions with dissimilar hardness that behave differently under the same stress regime can lead to deformation/ cracking in different regions. The main objective of performing this test study of welded joint twin discs is to observe actual defects in welded rails during service, such as cracking at HAZ ends and double squatting.

Mutton *et al.* [31] characterized a welded rail that underwent RCF in service and observed that the spheroidized region was more susceptible to crack nucleation.

However, there is a lack of research indicating the effect of rail HAZ microstructures on the propensity to develop RCF cracks. This study uses the twin-disc test to observe the effect of HAZ microstructure coming from a real mobile flash-butt weld.

2. Methodology

2.1. Material and welding process

The rail material used was a DHH Premium rail, commonly used in the Brazilian Heavy Haul railroads. The chemical composition and mechanical properties of the rail are described in Table 1. According to previous characterizations [10,11,20,32,33], although the chemical composition has a hyper-eutectoid chemical composition in wt%, the microstructure is completely pearlitic.

Table 1 – DHH Premium rail steel chemical composition in wt% and mechanical properties.

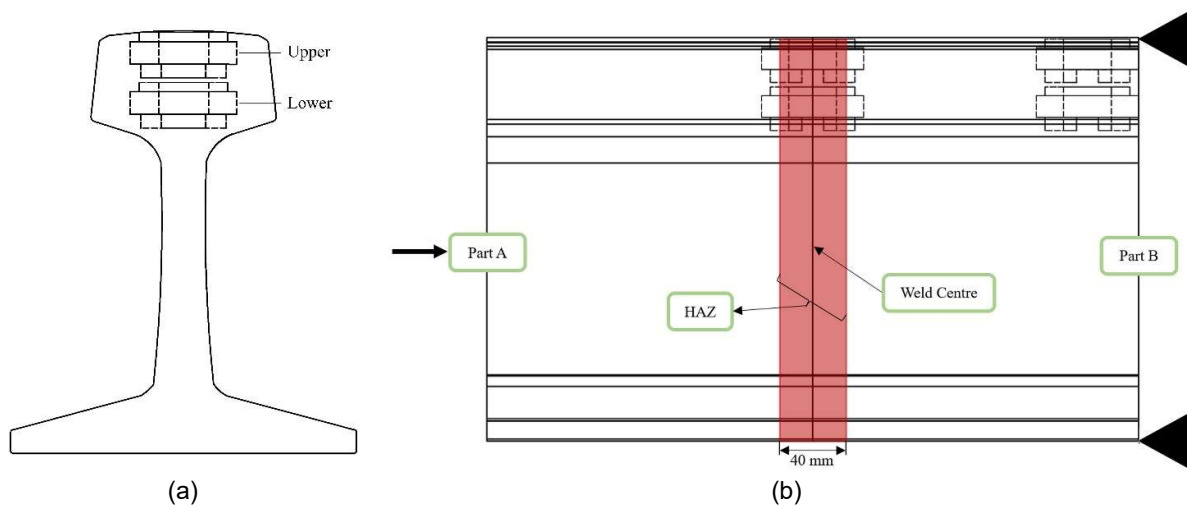| C	Si	Mn	P	S	Cr	Ys (MPa)	UTS (MPa)	El (%)
0.81	0.23	1.03	0.01	0.01	0.22	905	1160	9.8

The welding process was performed in Brazil according to the parameters currently used on Vale S.A. Heavy Haul railroads in Brazil. According to previous studies [10,11,20,32], the welding parameters met the HAZ length of approximately 36 mm and the samples were welded according to Table 2.

Table 2 – Welding parameters performed on DHH Premium rails.

Pre-flash	
Mean Voltage (V)	389
Mean Current (A)	380
Rail consumption (mm)	1.9
Duration (s)	30
Flash	
Mean Voltage (V)	356
Mean Current (A)	433
Rail consumption (mm)	10
Flash Velocity (mm/s)	0.05
Duration (s)	116
Boost	
Mean Voltage (V)	394
Mean Current (A)	230
Rail consumption (mm)	9
Flash Velocity (mm/s)	1.47
Duration (s)	9
Upset	
Rail consumption (mm)	15
Maximum Current (A)	937
Duration (s)	0.3
Forging	
Forging Force (t)	76
Duration (s)	2.01

2.2. Twin-disc test

Twin-disc tests were performed using the SUROS twin-disc machine [34] at The University of Sheffield to analyse the dry rolling contact fatigue (RCF) and wear resistance. The discs were machined in the horizontal direction from the DHH Premium rail, as shown in Figure 2-a. The discs were cut in such a way to have all the HAZ microstructures present, as shown in Figure 2-b. Therefore, up to two discs were removed from each welded joint. The "wheel" counter-discs were taken from the same base metal to have a standard material for all tests. The HAZ length had an overall length of approximately 36 mm, and the twin disc test specimen was 47 mm. This specimen extraction geometry was decided upon because this has both the A and B part softening regions, along with the central region. The disc considered as the rail rotated at a lower speed with 396 rpm (driven) than the disc considered as the wheel with 400 rpm (driving).
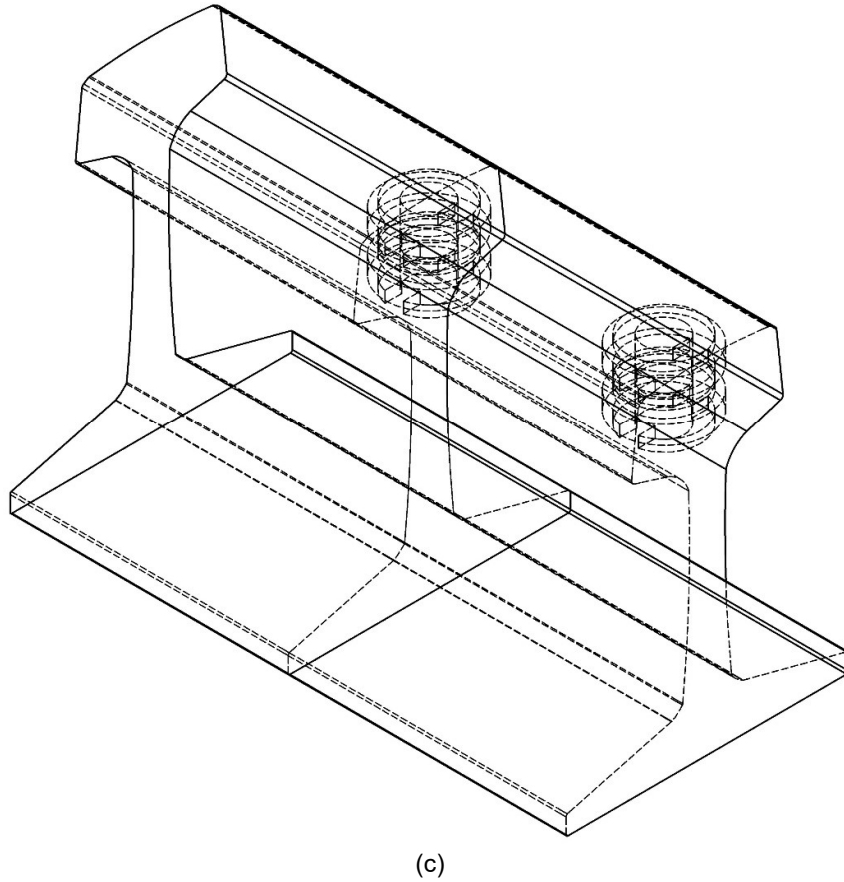

(a)   (b)

(c)

Figure 2 – Locations where twin-disc tests specimens were cut from the welded joint and base metal in the rail. In (a), the transversal section of the rail and the extraction site is observed, while in (b), the longitudinal section is depicted. In (c), the specimen extraction regions are displayed in an isometric view.

The maximum contact pressure was calculated according to the Timoshenko and Goodier [35] method. The maximum contact pressure in the interface between two cylinders with a radius (R_1 and R_2), the same elastic modulus (E) and Poison's coefficient (v) of 0.3 and P' is the normal load, can be described by equation 1.

$$P_0 = 0.418 \sqrt{\frac{P'E(R_1+R_2)}{R_1 R_2}} \qquad (1)$$

The parameters of the twin-disc tests are described in Table 3. These values were based on several references that used the twin-disc test to characterize and analyse the contact between rail and rail wheel [36–41]. The stopping point for the twin-discs tests was at a total of 30,000 cycles, and air was not employed to disperse the debris.

Table 3 indicates the utilization of 8 discs extracted from the Heat-Affected Zone (HAZ) region and 12 discs from the region outside the HAZ. This facilitated the conduction of tests employing the discs from the non-HAZ region as the base metal for simulating the wheel discs. Furthermore, tests number 9 and 10, corresponding to scenarios without

8

interference from microstructural gradients, were conducted using four discs from the non-HAZ region.

Table 3 – Twin disc test matrix with the location of each specimen, load, and slip.

Test	Disc 1	Disc 2	Po (MPa)	Slip (%)
1	HAZ (Part A and B) - Upper	DHH (Upper)	1100	1
2	HAZ (Part A and B) - Lower	DHH (Lower)	1100	1
3	HAZ (Part A and B) - Upper	DHH (Upper)	1100	1
4	HAZ (Part A and B) - Lower	DHH (Lower)	1100	1
5	HAZ (Part A and B) - Upper	DHH (Upper)	1500	1
6	HAZ (Part A and B) - Lower	DHH (Lower)	1500	1
7	HAZ (Part A and B) - Upper	DHH (Upper)	1500	1
8	HAZ (Part A and B) - Lower	DHH (Lower)	1500	1
9	DHH (Upper)	DHH (Upper)	1500	1
10	DHH (Lower)	DHH (Lower)	1500	1

2.3. Characterization

After the tests, the worn surfaces of the discs were preserved for analysis. The surface roughness of the discs was measured before and after the tests using a non-contact profilometer (Alicona Infinifocus®). Metrological variation analysis of the circumference of the discs was also performed using the Alicona Infinifocus® to highlight regions with higher/lower wear rates.

Topographic characterization of the disc after the wear test was performed with a laser scanner (Creaform HandyScan Black Elite®). Using this scanner, a set of reference points was positioned, enabling the three-dimensional reproduction of the discs in the software through a laser mesh. The comparison of the topography on the wear track between the two discs was measured radially from the centre of the two discs. The results were compared with a reference disc with a diameter of approximately 1 mm smaller. Thus, a comparison could be made with a colour chart to the reference disc, locating the regions that suffered more or less plastic deformation.

Wear was measured by mass loss, measuring before and after the twin-disc test on a precision balance. In each one of the measurements, the discs were cleaned with alcohol and demagnetized. Demagnetization is an important process to prevent interference with the sensitivity of mass weighing scales.

In addition, the worn surfaces of the discs and counter-discs were analysed via optical microscopy and scanning electron microscopy (SEM). SEM secondary electrons were used to check the surface topography to identify grooves, cracks, and/or wear marks. SEM backscattered electrons were mainly used for determining the presence of oxides on the surface.

The cross-section of the disc surfaces was prepared metallographically by grinding and polishing. Some samples were etched by immersion in Nital 2% solution for 30 s. Metallography of all regions, etched and non-etched samples, was observed by optical and scanning electron microscopy.

The hardness drop analysis for each HAZ edge was performed from hardness profiles. Two profiles were performed for each HAZ edge and each welding side. A micro-durometer Shimadzu HMV-2 was used with a load of 0.3 kgf for 15 s and a distance between indentations of 0.5 mm according to ASTM E92 [42]. The indented surface was polished to 1 mm, and the lowest hardness was compared to the base metal hardness. The base metal microhardness (upper and lower) was performed with 10 measurements each.

Nano-hardness tests were performed using a Bruker Hysitron Nano-Indentor® to verify the relationship between crystallographic aspects/directions and material hardness. For this, the same metallography samples were used, but polished with a colloidal silica solution of 0.05 μm. Eleven measurements were taken at intervals of 12.5 μm up to a depth of 500 μm from the surface.

3. Terminology

In the case of flash-butt welding of rails, there are two regions of decreasing hardness compared to the base metal, and adjacent areas, these being the central region and at the edges of the HAZ. In the central area, pro-eutectoid ferrite is formed due to the decarburization of the face to be welded during the process. The product of the welding process's thermal cycling and thermal partitioning gives rise to a microstructure gradient along the HAZ. At the edges of the HAZ, the temperatures reach the inter-critical region between Ac1 and Acm, which favours the cementite's spheroidization. In both cases, there is a considerable hardness drop compared to the original and pearlitic microstructure. The temperatures Ac1 and Acm denote critical points in phase transformations. Upon heating, as the pearlite stability field (Ac1) is surpassed, ferrite and cementite undergo a transformation into austenite. In the case of hyper-eutectoid steel, an equilibrium field forms between cementite and austenite, reaching a critical temperature (Acm) during heating. Beyond this temperature, only the austenite phase remains.

Plastic deformation was observed in all HAZ edge regions, and a valley was visibly observed, as shown on Figure 3. This more significant deformation in these regions is probably due to the hardness drop in these regions. The valleys in Figure 3 are deliberately

exaggerated and not to scale to facilitate a clearer visualisation of the phenomenon. As we will later discover, these valleys have a depth of less than 1 mm.
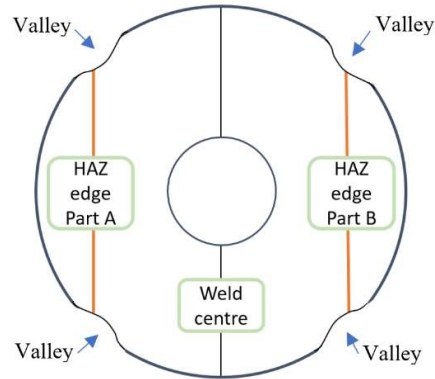

Figure 3 – Schematic representation of the valleys formed after the twin disc test coinciding with the HAZ edges.

During the tests, after the twin disc test, at least one of these two characteristics was observed in all regions of the HAZ edges and the central area of the weld:

- A considerably large crack, visible to the naked eye from a surface perspective (see Figure 4);
- A larger cluster of smaller cracks, but concentrated in this region, also from a surface perspective (see Figure 4).

It is worth mentioning that these classifications were performed from a superficial perspective. Subsequently, it was analysed that it was a crack (or a planar defect with crack characteristics).
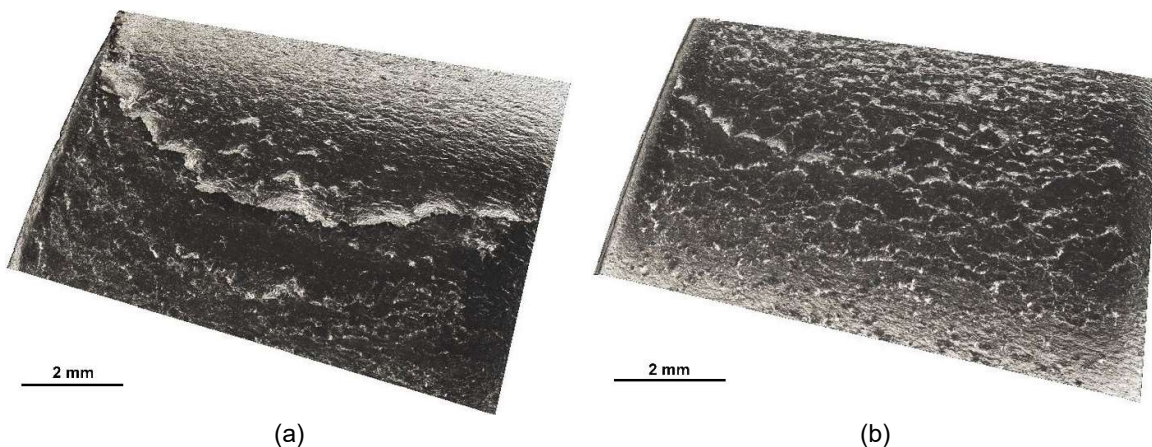

(a)   (b)

Figure 4 – Surface analysis obtained by Alicona Infinifocus® showing the two possible characteristics observed on the surface of the specimens after the twin disc test: (a) example of master crack observed on Test 5 specimen T1 and (b) example of higher concentration of surface cracks observed on Test 6 specimen T2.

As an analysis of all these crack areas was performed, for the regions where the largest cracks were observed, named master cracks (T1, T2, T3, T4, T5, and T6), only this

crack was considered, although there were other considerably smaller cracks in the adjacent areas. For the regions where a more significant number of concentrated cracks were observed in these respective areas, an average and standard deviation were performed considering all the cracks observed in the metallographic analysis. The regions of base metal were named as M1 and M2. Thus, the terminology was considered, as illustrated in Figure 5.
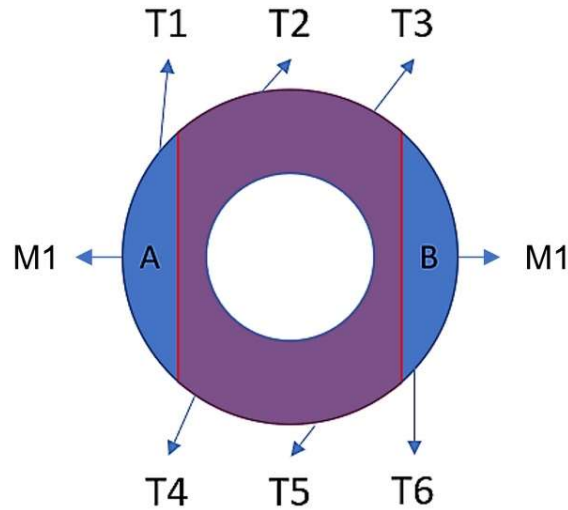

Figure 5 – Different regions observed on the disc containing all the weld HAZ regions and their specific terminology.

The other regions, for example between T1-T4 and T3-T6, showed a concentration of cracks not visible to the naked eye. As these regions were not the focus of this study, they were not analysed in depth.

4. Results

4.1. Hardness tests

The average base metal hardness of the specimens taken from the top of the rail head was 378.1 (19.1) $HV_{0.3}$. At the same time, the specimen's base metal hardness extracted from the bottom of the rail head was 339.9 (15.6) $HV_{0.3}$. It was an average reduction of approximately 10%. These values were probably due to the lower region's lower cooling rate of the rail head relative to the distance from the heat-treated surface.

Two hardness profiles were performed for each weld and each weld side, as described in Figure 1. These results show a minor difference in hardness concerning the height of extraction of the specimens. In contrast, a relationship between the hardness drop as a function of the welding side was not observed. The results of the hardness difference

between the average of the lowest hardness value presented in the HAZ and the average hardness of the base metal are described in Table 4.

Table 4 – Hardness drop as a function of specimen extraction height and welding side.

Hight	Side	Hardness drop	Standard deviation
Upper	A	31.9%	1.8%
Upper	B	33.2%	1.6%
Lower	A	24.3%	1.6%
Lower	B	25.2%	1.7%

4.2. Mass loss analysis

The results of the total mass loss after the wear tests can be seen in Table 5. Two characteristics can be clearly observed: Tests 1 to 4 showed less mass loss compared to tests 5 to 10 and the "rail" discs showed less mass loss than the "wheel" counter-discs. Furthermore, it is possible to qualitatively state that, on average, the discs removed from the top ("upper") lost more mass than those removed from the bottom of the rail ("lower").

Table 5 – Gross mass loss of each disc after the twin-disc tests.

Test	Specimen location	Rail disc (g)	Wheel disc (g)
1	Upper	0.2451	0.2454
2	Lower	0.2601	0.2735
3	Upper	0.2520	0.2533
4	Lower	0.2479	0.2524
5	Upper	0.5761	0.656
6	Lower	0.4119	0.6296
7	Upper	0.5178	0.5652
8	Lower	0.4089	0.5329
9	Upper	0.4212	0.4666
10	Lower	0.4706	0.5656

By refining the results as a function of mass loss per test cycle, the graph in Figure 6 was plotted. As detected earlier (Table 5), the mass loss of the samples tested at 1100 MPa was considerably lower compared to the samples tested at 1500 MPa. For all tests, the mass loss of the discs (rail) was lower than the counter-disc (wheel) for the samples tested at 1500 MPa.
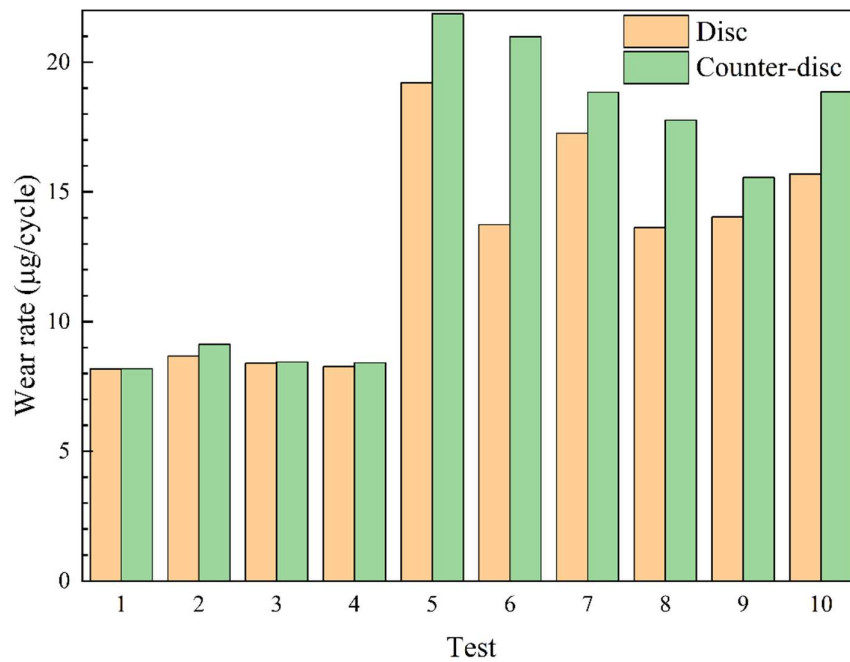
Figure 6 – Wear rate of each of the twin-disc tests. The presented results do not include standard deviations as they represent raw data obtained from each of the rolling/sliding wear tests.

The word specimen set was used to refer to both the disc and the contradictor (rail and wheel). When comparing the tests performed at 1500 MPa with upper discs (Tests 5, 7, and 9), it can be clearly seen that the welded specimen sets lost more mass than the specimen set taken from the base metal with the same distance from the surface. Although a similar pattern was not observed in tests conducted at 1500 MPa using lower discs (Tests 6, 8, and 10).

4.3. Coefficient of traction

The relationship between the Coefficient of Traction (COT) and the maximum contact pressure is shown in Figure 7. There was little variation between the tests performed at 1100 MPa. The standard deviation of both the maximum contact pressure axis and the COT axis were very close to each other. The COT results varied a little from the tests performed at 1500 MPa. The average COT of the tests performed at 1500 MPa was higher than those performed at 1100 MPa.

The average COT of the base metal tested at 1500 MPa of the specimen taken from the upper part of the rail head was lower than the average of the specimen taken from the lower part. The same behaviour does not hold for the upper and lower welded specimens. The specimens taken from the upper welded region showed higher average COT when compared to the specimens from the lower welded region.
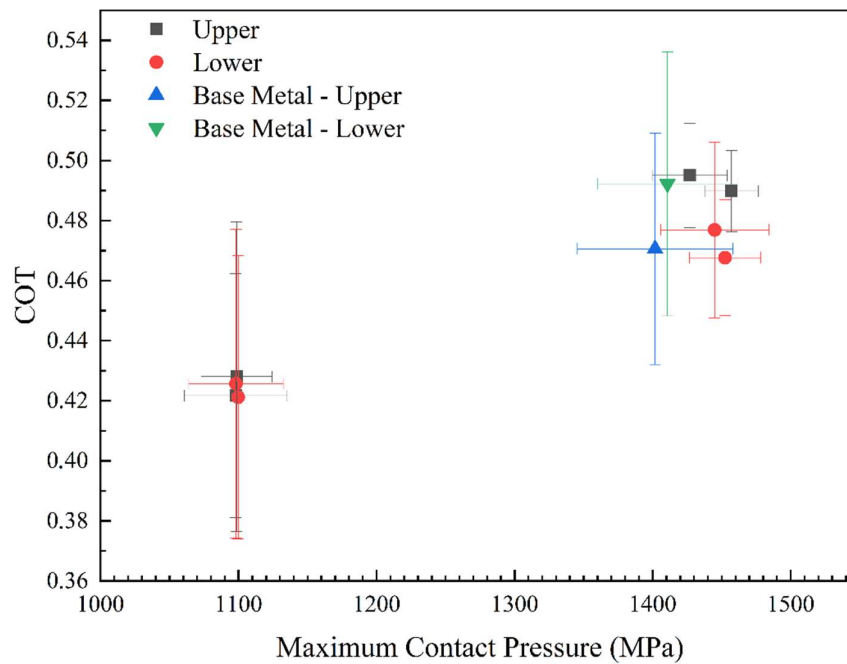
Figure 7 – Coefficient of Traction (COT) against maximum contact pressure from the SUROS twin-disc tests. The averages and standard deviations of both the load fluctuation and the coefficient of traction (COT) throughout the entire test duration are plotted.

4.4. Topography analysis

The macro-topography analysis can be seen in Figure 8. Two discs containing all HAZ microstructures and tested at 1500 MPa were analysed. Compared to a reference disc, it is noticeable that there is a difference of more than 0.5 mm visibly in two regions. These regions coincide exactly with the cementite spheroidization region. This statement was possible due to the markings on the specimen identifying the weld centre and hardness drop regions characteristic of rails flash-butt welding.

The specimens tested at 1100 MPa did not present a deformation as evident as the tests performed at 1500 MPa. Also, the upper specimen showed greater deformation width (green part) than the lower specimen, suggesting that the difference between the hardness significantly affected this local deformation.

All the discs, including the wheel counter-discs, were analyzed. However, only the most pertinent results are presented in the figures, while the overall findings are described in the text. Given that the discs with the microstructural gradient of the weld were the primary focus of the study, both the results and discussions are centred around them. While acknowledging that microstructural variations in the counter-disc could potentially influence the results, a deliberate choice was made to employ the same microstructure as the base metal. This decision aimed to minimize test variables and ensure more uniform results. It is

15

worth noting that the AAR standard [43] itself recommends utilizing the material itself as a counter-disc.

A Python programme [44] was developed to extract topography data for assessing its correlation with disc radius, aiming to validate alterations post-tests. Although the programme was developed to cater to image analysis requirements, it requires refinement. Nonetheless, significant insights were gleaned. Notably, in Test 5, bulges measured approximately 160 microns, whereas in Test 6, they diminished to around 120 microns. As research progresses and more tests are conducted to attain a robust statistical understanding of disc behaviour, enhancements will be made to the programme to furnish more accurate measurements for each region exhibiting significant deformation in the tested discs.
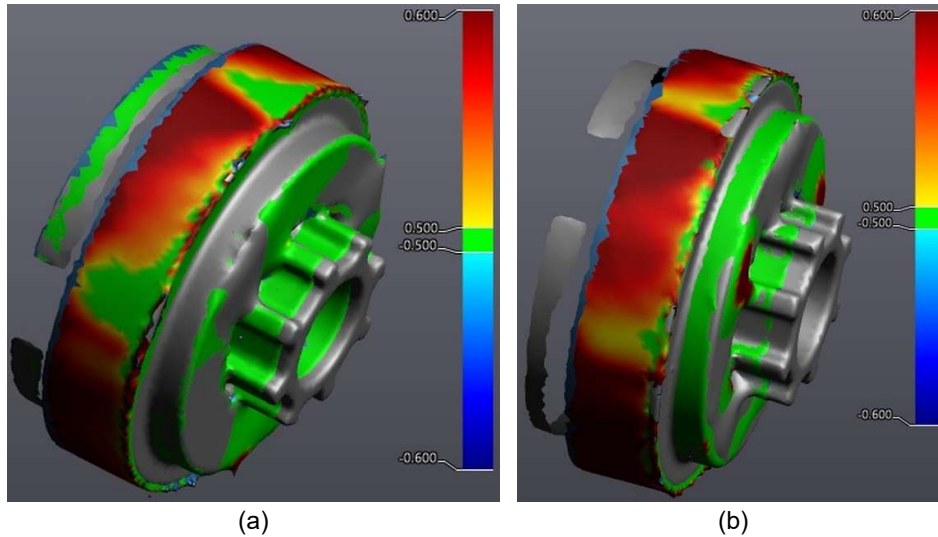

(a) (b)

Figure 8 – Macro-topography analysis of two discs containing all HAZ microstructures and tested at 1500 MPa from Tests 5 and 6: extracted from the upper (a) and from the lower (b) part of the rail head. All units in mm.

The surface microtopography before the test is represented in Figure 9. The machining grooves are in the direction following the wear test track. The average Ra before the test was 0.698 μm. The micro-topography of the rail part surface specimen extracted from the base metal at the top of the rail head is shown in Figure 9, and the one taken from the bottom is shown in Figure 9. A change in morphology after wear is evident. The wear surface shows flakes across the wear test track, indicating the presence of rolling contact fatigue cracks. The average Ra after the twin-disc test was 0.392 μm for the upper specimen and 0.581 μm for the lower specimen.

16

(a)   (b)   (c)
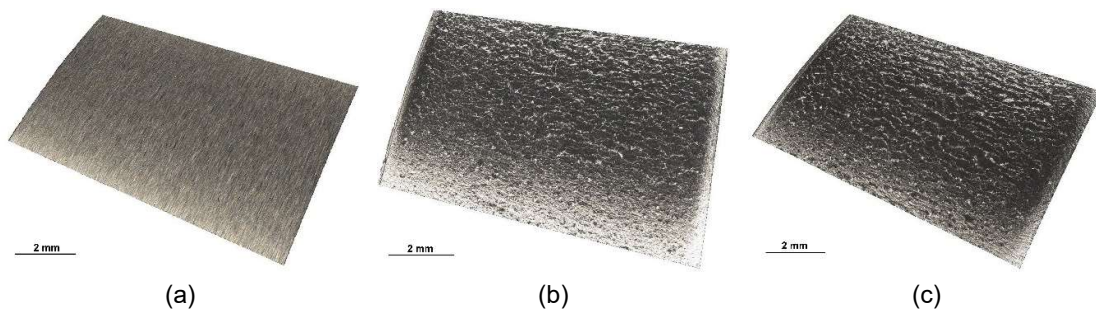
Figure 9 – Micro-topography analysis of test wear test track from the before test disc (a) and after the test from the discs extracted from the upper (b) and from the lower (c) part of the rail head.

The microtopography was analysed in the regions just before the great crack or area with an RCF crack concentration (T1, T2, T3, T4, T5, and T6). The base metal regions of the discs containing the weld were also analysed, named M1 for the base metal of part A and M2 for the base metal of part B. A graph was assembled with the values were divided into load and height of specimen extraction:

- The regions of cracks T1 and T4 and base metal M1 correspond to side A;
- The crack regions T3 and T6 and base metal M2 correspond to side B;
- While crack regions T2 and T5 correspond to the weld centre region.

The results are shown in Figure 10. A drop in Ra is observed sharply in the region of spheroidization (A and B). There is also an increase in Ra in the central region. These two previously mentioned characteristics are repeated in all tests performed. With this separation, the visualization of the results becomes more didactic.

These tests show that Ra is elevated in the region of the base metal, and the results of the tests performed at 1100 MPa with specimens extracted from the lower part of the rail head stood out. A considerable elevation of the Ra in the test performed at 1500 MPa of the specimen extracted from the lower part of the rail head is noteworthy. In contrast, the test performed at 1500 MPa of the specimen extracted from the upper part of the rail head showed an increase of Ra in the central region, but not pronounced in the base metal region.
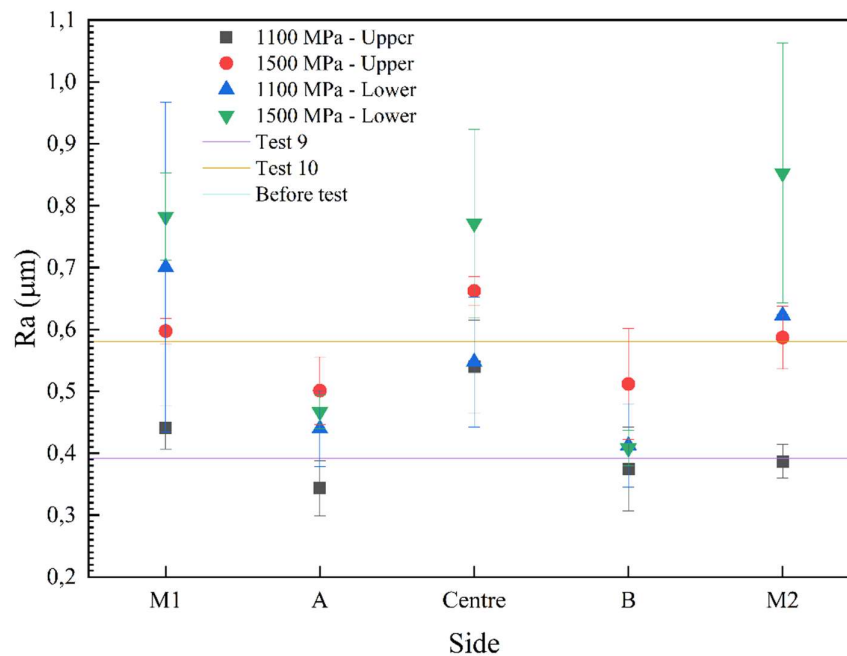
Figure 10 – Surface Roughness (Ra) distribution just before each critical region is described in Figure 5. The means and standard deviations of the distribution of Ra measurements are depicted on the graph

4.5. Microstructural analysis

Almost all specimens observed a master crack in the weld centre. An example of the micrography of the cross-section of Test 2 T2 is shown in Figure 11. A more prominent crack than the adjacent cracks is observed in the left part of Figure 11. By following the strain line of the end of the crack, it is possible to see that it is tied precisely to the region with the presence of pro-eutectoid ferrite. This relation is surprisingly exact: precisely in the ferrite area, it follows the deformation, a "delamination" occurs, and finally generates a crack-like defect. All the other master cracks observed in the centre of the weld presented similar characteristics.
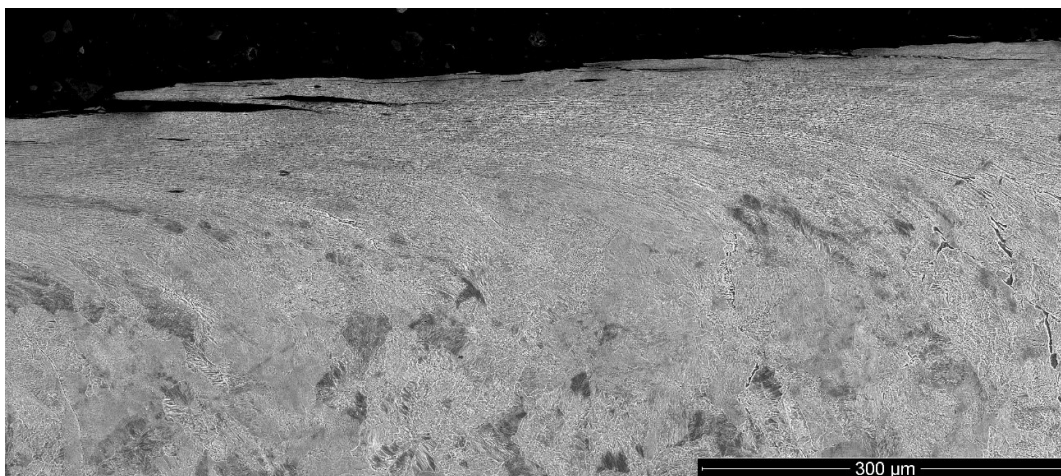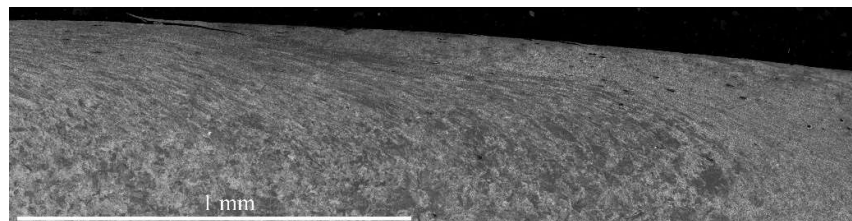
Figure 11 – Cross-section of an example specimen after the twin-disc test observed in the central region (Test 2 T2). The crack tip coincides precisely with the pro-eutectoid ferrite position located at the micrograph's far right side.

The cross-section of four examples of master cracks from the four test conditions with specimens containing the weld is shown in Figure 12. All of the observed non-centrally located master cracks, although they were located just in front of the HAZ boundary regions, had the same characteristics:
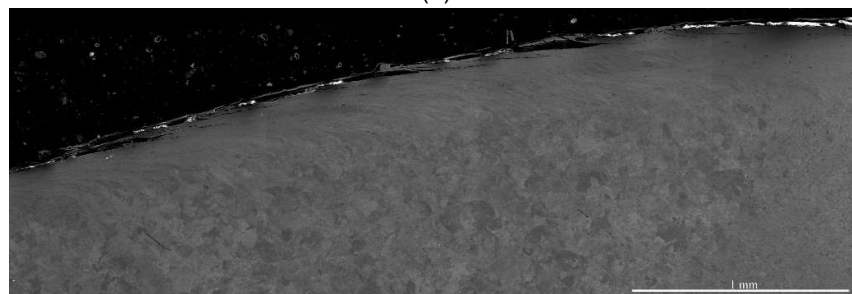
- They were the largest cracks (or crack-like discontinuity) in the area;
- They are linked with the spheroidization site of cementite (location of the HAZ edges of rail welds);
- The upper crack-like discontinuity region has a more spheroidized microstructure than the lower part.

The spheroidization regions of the cementite are located in the right area of Figures 12-a to 12-d. The crack tip and direction of propagation of the master cracks are perfectly aligned with the strain direction generated from the contact between the discs during the twin-disc test.
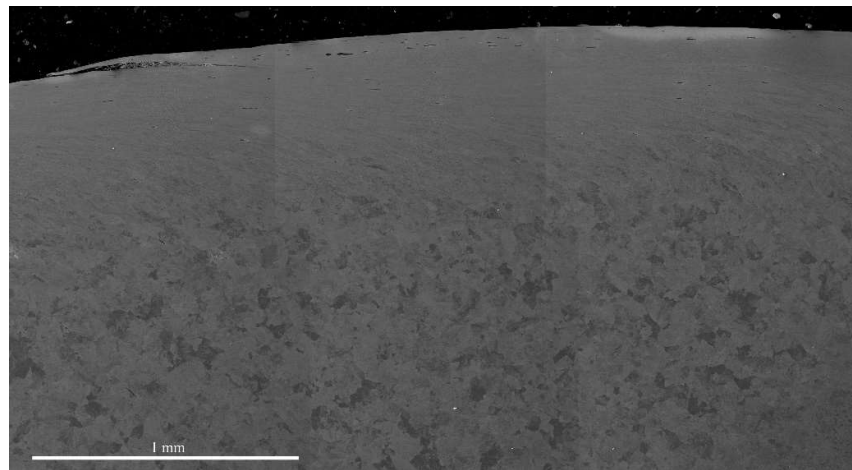
Another characteristic observed is that the spheroidization region presented a greater strain distance than the other regions with pearlitic microstructure. This characteristic, although observed in all master cracks, is more visible in Figure 12-a.
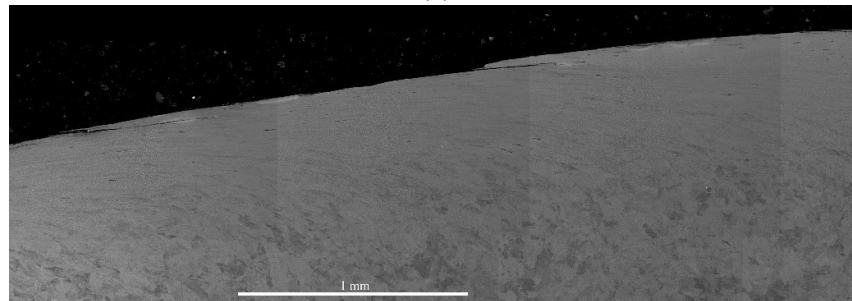

(a)

(b)

(c)

(d)

Figure 12 – Cross-section macrograph of specimens after the twin-disc testing. Four examples of master cracks and the relation of the crack to the HAZ edge microstructure are shown in each of the parameters: (a) Test 1 T1, (b) Test 2 , (c) Test 5 T1 and (d) Test 8 T4.

Some master cracks contained some particles inside. This characteristic is most evident in the Test 8 T4 sample shown in Figure 12-d. Some other master cracks also had this characteristic. A more enlarged image of this feature is shown in Figure 13. According to Figure 13-b, these larger particles are steel with spheroidized microstructure from the rail itself. EDS analysis showed that the smoothest part (located at the red marking in Figure 13-b) has a large amount of oxide (see Figure 13-c). Oxides formed during wear and were subsequently entrapped by the extrusion surface deformation. This was confirmed by a basic SEM surface analysis, which revealed the presence of oxides after the rolling/sliding wear test. This oxide formation indicates that this surface has been worn down due to the contact between discs leading to oxide formation. Subsequently, this region has been engulfed by the deformation of the less hard microstructure. These characteristics suggest that the "master crack" is the product of extrusion and not RCF.
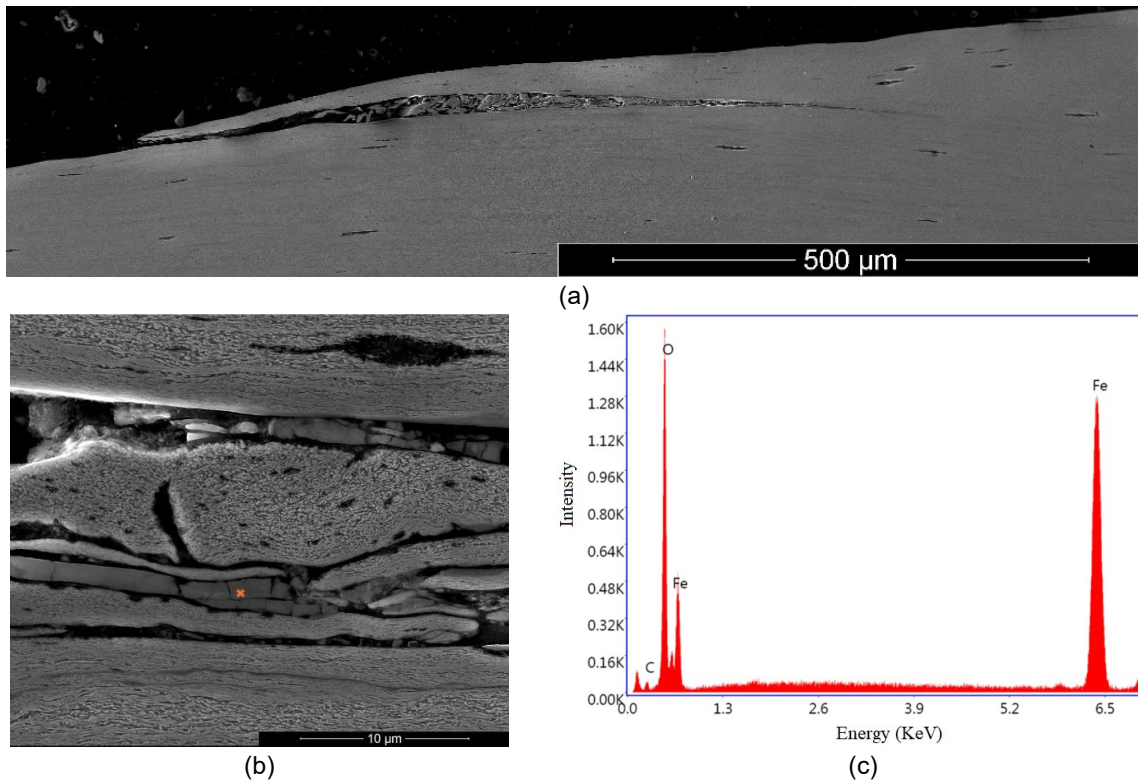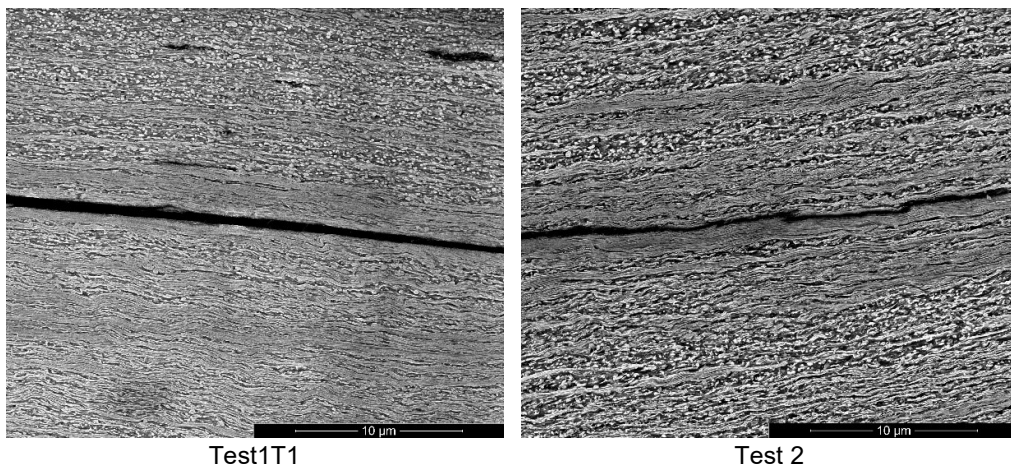
(a)

(b)

(c)

Figure 13 – (a) Master crack of Test 5 T1 showing debris within the crack. (b) More detail of the debris in the middle of the crack shows that the debris's microstructure is spheroidized cementite and the EDS analysis site. (c) EDS analysis shows that this is a region of oxide.

Figure 14 shows four master cracks observed at each tested condition: 1500 MPa, 1100 MPa, upper and lower discs. As mentioned earlier, the upper region of the crack showed spheroidized microstructure, while the lower part of the crack has more pearlitic lamellar microstructure. The crack presents straight, unbranched characteristics and follows the deformation lines. The pearlite lamellae are entirely aligned with the deformation of the disc contact, and the crack runs parallel to this alignment. The surfaces in Figure 12-a and 12-c present a smooth surface, while Figure 14-d presents a slightly rougher surface. EDS analysis showed the presence of oxide in all cracks analysed by SEM.
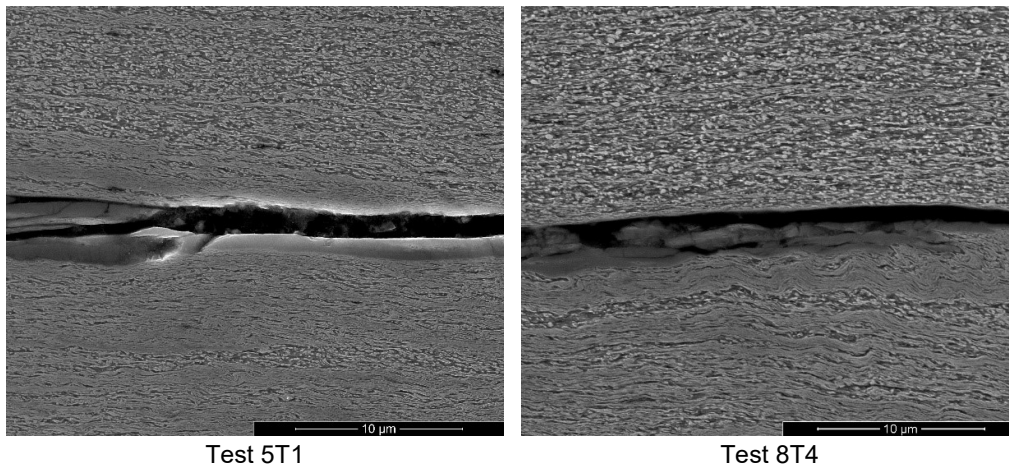

Test1T1

Test 2

Test 5T1   Test 8T4

Figure 14 – Cross-section micrograph of the specimens after the after twin-disc test. Four examples of master cracks are shown in each of the parameters: (a) Test 1 T1, (b) Test 2, (c) Test 5 T1, and (d) Test 8 T4. It is noted that the upper microstructure is more spheroidized than the microstructure below the crack.

4.6. Crack dimension analysis

The length and depth distribution of the cracks observed in each region are presented in Figure 15. Despite a higher average length and depth of the 1500 MPa lower test condition for side B, it was not possible to observe a clear difference between the cracks and the A and B sides.

For the base metal, a quarter of the longitudinal section of the disc was removed, and the length and depth of all cracks were contacted. The average crack length and depth for each condition is identified in Figures 15-a and 15-b as the yellow and blue lines. Clearly, there is a tendency for the cracks in the specimens taken from the lower region of the head rail to be larger and deeper than the cracks in the specimens taken from the area closer to the surface (upper).
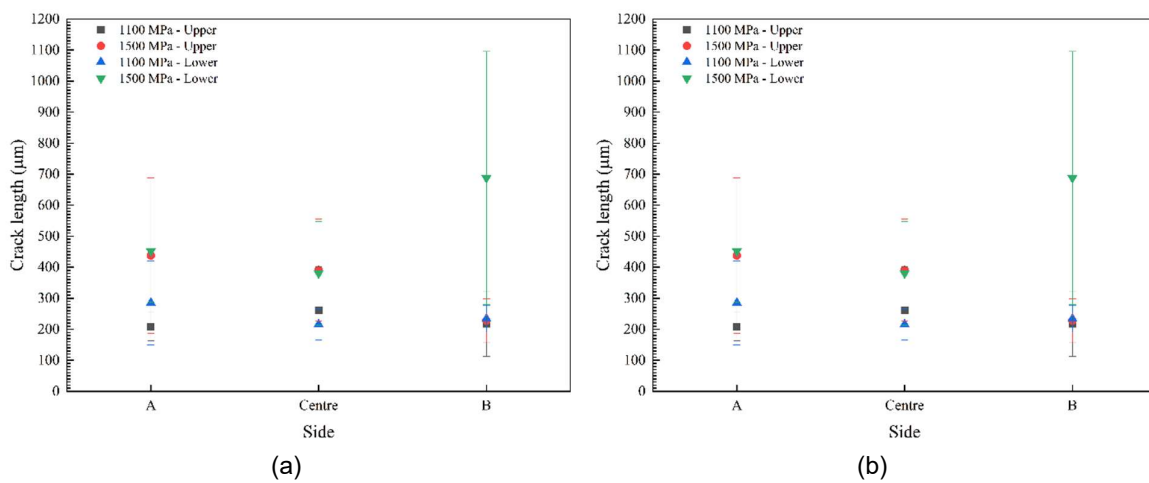

(a)   (b)

22

Figure 15 – The crack length and depth distribution for each condition for each weld centre and HAZ edge in each side. The means and standard deviations of the measurements of the size of the RCF cracks and/or master cracks are displayed on the plot.

The nanohardness results of test 5-T1 and test 8-T3 are depicted in Figure 16. The mean and standard deviation of each of the eleven measurements at the centre of the calculated mesh along the distance from the surface are displayed. It is noted that the hardness increases as it approaches the surface between 750 HV and 800 HV until it approaches the crack. Between the crack and the surface, there is a slight drop in hardness followed by a sudden increase, reaching between 900 HV and 1000 HV.
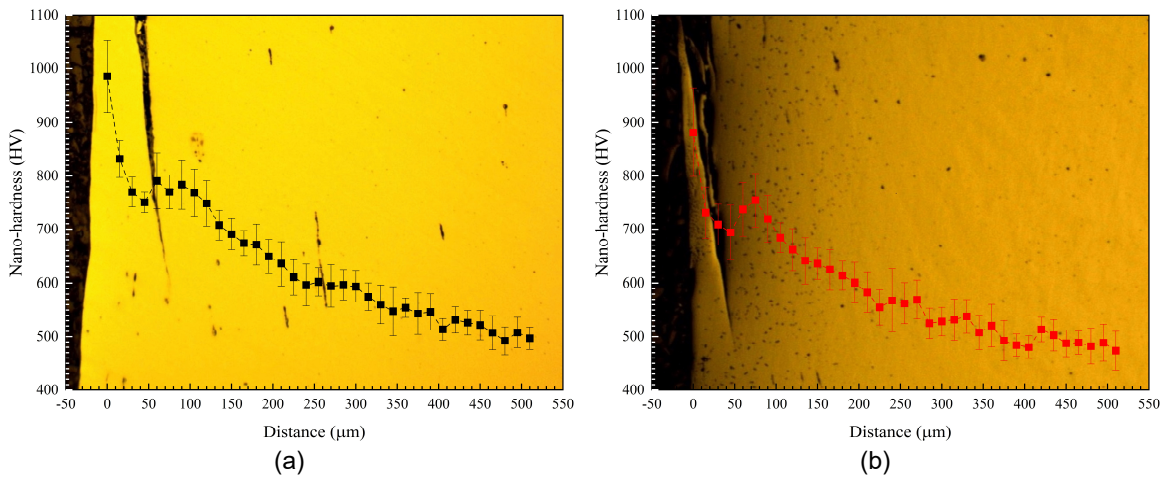

(a)   (b)

Figure 16 – Nanohardness profile of (a) Test 5-T1 and (b) Test 8-T3. The means and standard deviations of the nano-hardness measurements are presented on the plot.

5. Discussion

The twin-disc test using a welded joint with all microstructures in the flash-butt welding process is a new test. Although this is a new test, much information has been extracted that will allow us to better understand the phenomena involved in crack formation and wear in the welded rail area. First, it was possible to recreate on a laboratory scale a type of defect commonly observed in the field: double squat-like defects in the softest microstructure region. Other phenomena like changes in Ra and the genesis of crack formation in the softer areas were also observed. As this is a new test, more experiments should be performed for a better understanding and statistical representation of the results.

Upon reflection on the test, certain limiting factors became apparent, including constraints related to specimen extraction and their height relative to the surface. Relying solely on mass loss and surface analysis might prove inadequate for a comprehensive

assessment, warranting an in-depth examination of the softened regions. A potential avenue for future research on the same topic would involve conducting additional tests, with an aspiration to isolate microstructures to scrutinize their behavior independently of the microstructural gradient. Another aspect worth investigating could be the correlation between diverse materials designated as the counter-disc. This may involve materials extracted from railway wheels with distinct microstructures, such as bainite and pearlite, for instance.

The formation of master cracks (or RCF crack concentration) precisely in the region of the softer area drew a lot of attention in all specimens. It was evident that there were at least six regions with a greater propensity to crack formation. This information is similar to that observed by Mutton *et al.* [31] in their analysis of extracted rail, cracking was observed mainly at the ends of the HAZ in the cross-section metallography.

In their study, Mutton *et al.* [31] observed a network of carbides in former austenitic grain boundaries just after the HAZ softening. This same ex-service rail has a carbon equivalent of about 1%. This amount of carbon prevents decarburization in the central region to the point of forming pro-eutectoid ferrite, as observed by Bauri *et al.* [10]. This lower tendency to form pro-eutectoid ferrite is also observed in the hardness profiles of the ex-service rails, in which there is no evident hardness decrease in the central area of the welds. The formation of pro-eutectoid ferrite is common for steels with equivalent carbon closer to the eutectoid equilibrium and has been observed by several authors [10,21,23].

This higher amount of carbon equivalent also makes the steel more prone to form cementite at the previous austenite boundary. It was observed by Bauri *et al.* [10] that the rail with higher carbon content presented a fragility precisely in the region adjacent to the softening. Even in their research, tensile tests showed greater fragility precisely in this region.

Analysing the mass loss (Figure 6), firstly, we must analyse the data from Test 9 and Test 10. These tests were performed with unwelded specimens as a reference for the tests performed at 1500 MPa. Test 9 showed a considerably lower mass loss than Test 10. This lower mass loss is due to the rails being treated at the head, generating greater hardness on its surface but not reflecting in its core. Thus, a microstructural heterogeneity is generated, which decreases its hardness as the distance from its original surface increases. It is well-established that there is an inversely proportional relationship between hardness and material loss due to wear [4]. Furthermore, a lower cooling rate delivers a lower pearlite

lamellae width [45,46]. The distance between the pearlite lamellae directly influences wear and RCF formation [41].

The mass loss of the driving disc, identified as the wheel disc in this study, exceeded that of the driven disc, which was the rail disc in this investigation. The observed pattern of higher mass loss in the driving discs has been thoroughly discussed, as demonstrated by studies conducted by Hu et al. [47] and Ding et al. [48]. The study conducted by Hu et al. highlighted that, with the same material and initial hardness ratio, the driving disc exhibited a greater mass loss. Also, It was observed that with a slip of 1%, the driving disc underwent more substantial plastic deformation and exhibited less work hardening when contrasted with the driven disc. Ding et al. conducted numerous twin-disc tests using the original rail and railway wheel materials. They noted a distinction in the wear mechanisms between the two components. Fatigue and severe wear were observed on the (driving) wheel, while peeling and spalling occurred on the (driven) rail, particularly under high loads and severe wear conditions. Although the counter disc exhibits greater homogeneity and hardness than the main disc in certain regions, there is still a propensity for both cracking and mass loss in the driven disc. Pereira *et al.* [30] also observed this behaviour: even when testing with pearlitic counter-discs against with spheroidized cementite with lower hardness, the counter-discs presented a higher cracking tendency. For tests with discs of the same microstructure, the greatest loss of mass was found in the counter-discs.

For the tests performed at 1100 MPa, the lower specimens showed higher mass loss than the upper specimens. In contrast, with the welded specimens tested at 1500 MPa, the mass loss of the lower specimens was lower than the upper specimens. This behaviour can be explained by the difference in hardness between the base metal and the HAZ softer region, as presented in Table 4.

The multiple regression to predict the load (MPa), COT, hardness-loss (HL), and specimen location (SL), ranging between 1 for upper and -1 for lower, are presented in Equation 2. The ideal scenario would be to perform more tests with the same parameters, but it isn't easy to obtain specimens, although the R^2 was 0.9501, demonstrating the high regression reliability in predicting the mass loss. Nevertheless, tests with the same parameters and different welding tracks/parameters will be performed in future works.

$$\text{Wear} = -44.8 + 0.00233 \cdot \text{Load} + 117.2 \cdot \text{COT} + 3.14 \cdot \text{HL} + 0.364 \cdot \text{SL} \qquad (2)$$

One characteristic observed is the regression's significant relationship between COT and mass loss. The effect of COT on wear is known and can be described as the Tγ number

in the various known wear prediction equations [49–51]. T is the test tractive force (normal traction force coefficient), and γ is the creepage.

Two softer regions are more prone to deformation compared to adjacent harder areas. This deformation can be classified as squat-like defects [52]. According to Steenbergen and Dollevoet [52], this microstructural, and therefore hardness heterogeneity, forms a non-uniform shakedown. This localized deformation was also observed by Mutton *et al.* [31] Two depressions were observed, followed by cracks in the ex-service rails.

Twin-disc tests performed with specimens containing the weld showed the same effect (see Figure 8). Two regions with higher deformation precisely in the spheroidization region of the HAZ. No deformation was observed in the central area of the weld. Therefore, it was possible to reproduce a real defect in laboratory-scale twin-disc testing.

The evident deformation observed mainly in the specimens tested at 1500 MPa suggests that it may cause lower COT than the tests performed at 1100 MPa (see Figure 7). This increased deformation is also linked to the formation of master cracks observed in all regions with lower hardness and in the centre region of the weld. With lower pressure (1100 MPa), there was less tendency for deformation of the softened regions, and in several cases, no master cracks were observed for this test pressure condition.

There is an apparent decrease in Ra just before the master cracks (sides A and B), as seen in Figure 10. There is a homogeneity of Ra in adjacent areas, such as the centre and base metal. This decrease in Ra indicates some phenomenon involved with the deformation of the spheroidized (less hard) region. Apparently, the deformation observed in the valleys formed at the edges of the HAZ (see Figures 3 and 8) decreased the cracking trend and favoured deformation in the adjacent area for this specific microstructure. This characteristic of increased deformation propensity and decreased roughness in twin disc tests with spheroidized microstructure was also observed by Pereira *et al.* [30]. The lower Ra on the A and B sides (Figure 10), the large deformation in the squat-like defect region observed in Figure 8, and the master cracks (Figure 12) are closely linked. The relationship of the heterogeneous microstructure (spheroidized HAZ and pearlitic cementite) to the master cracks is evident in Figures 12 and 13.

The central region of the weld showed pro-eutectoid ferrite common in flash-butt welding [10,23]. The deleterious effect of pro-eutectoid ferrite on RCF resistance is known and very well documented [1,53]. By analysing Figure 11, the exact position where the crack propagates is the deformation line where the pro-eutectoid ferrite nucleated in the former

austenitic grain boundary is located. As all discs showed master cracks or higher concentrations of RCF cracks in this region, this only proves this deleterious effect.

An analysis by Cvetkovski *et al.* [54] found particular metal inside the crack. It was observed that the crack is not only stressed in mode I, but also in shear mode II or III [55]. The two surfaces keep touching each other and acting under stress. These stresses can be the origin of the particles observed in Figure 13, in which the material near the surface crushes the material boundary forming flakes inside the crack. Another factor is the cracking of oxides by the same process. The origin of the oxides observed in Figure 13 is different because the test was dry. Still, the oxide cracks transverse to the crack surface can be originated by the same reason of efforts also in modes II and III. In the case of Cvetkovski *et al.* [54], used railroad wheel steel was analysed, which suggests that it has been weathered by the environment, such as rain and moisture cycles.

To investigate the formation of oxide on the surface, a comprehensive surface analysis was conducted using backscattered electrons in the SEM, revealing distinct regions enriched with oxide, notably concentrated along one of the primary cracks. EDS analysis was subsequently performed on these darker regions, conclusively confirming their composition as oxide-containing surfaces. Consequently, it was determined that the presence of oxide within the primary cracks resulted from wear and was subsequently incorporated through the extrusion deformation of the less resilient microstructure.

When comparing this feature with the macrographs in Figure 12, it can be seen that the spheroidized region presents a longer elongation length on the surface when compared to the adjacent area. The more significant deformation and the harder surrounding microstructure can form a crack-like defect by plastic ratchetting [56]. The master cracks formed by differential deformation between the spheroidized part, and the pearlitic part closely follow the preferential direction of the microstructure [57].

Surface deformation, especially at higher loads, causes the formation of these planar defects by extrusion of the less hard microstructure above the harder microstructure. This planar defect can generate a concentration of stresses in the face of the actuating contact stresses [58].

In a more practical way, by transferring the data obtained in the twin-disc test of the welded joints to an actual wheel-rail contact situation, this planar defect can evolve to low cycle fatigue crack propagation following the microstructure contour. The contact stresses between the wheel and rail or the rails bending during operation can lead to the propagation

of these defects in such a way as to fracture the rail with the train derailment as a possible consequence.

In the Handbook of Rail Defects [59], there are at least two examples of transverse cracking that occurred where nucleation occurred just at the transition of the HAZ of the welded joint. Considering this context, the importance of obtaining welding parameters that reduce both the decrease in hardness and mechanical properties of the welded joint and rails with less tendency to spheroidization at the limits of the HAZ is verified. These conclusions were also observed by Saita *et al.* [22], Alves *et al.* [20], and Bauri *et al.* [10].

The presence of oxide inside the master cracks makes it clear that there is oxidation formation during contact between the discs during the test, and then this surface is covered by the less hard HAZ region (see Figure 12 and 13). Although somewhat different from the present case, microstructural heterogeneity was observed by Mesaritis *et al.* [60]. it was observed that less hard microstructures could cover harder microstructures. In this case, WEL was observed covered by the base metal during sliding.

It is worth noting that taking the specimen further from the surface increases both the length and depth considerably. The average crack length of the upper (Test 9) base metal specimen was 85.0 (14.3) µm, and the lower (Test 10) was 184.8 (69.5) µm. While the crack depth of the base metal specimen upper (Test 9) was 12.0 (2.6) µm, and the lower was 18.0 (2.7) µm. As a technological consequence, it is evident that the worn rail with a smaller original section after a period of service has a significantly lower wear resistance/RCF. Additionally, the observed master cracks averaged substantially higher than the respective RCF cracks of the base metal (see Figures 11, 12 and 13).

Furthermore, there is a direct relationship between the length of the observed cracks and their depth and can be observed in Figure 17. There is a range of behaviour between both depth and length. The larger the planar defect, the greater its depth.
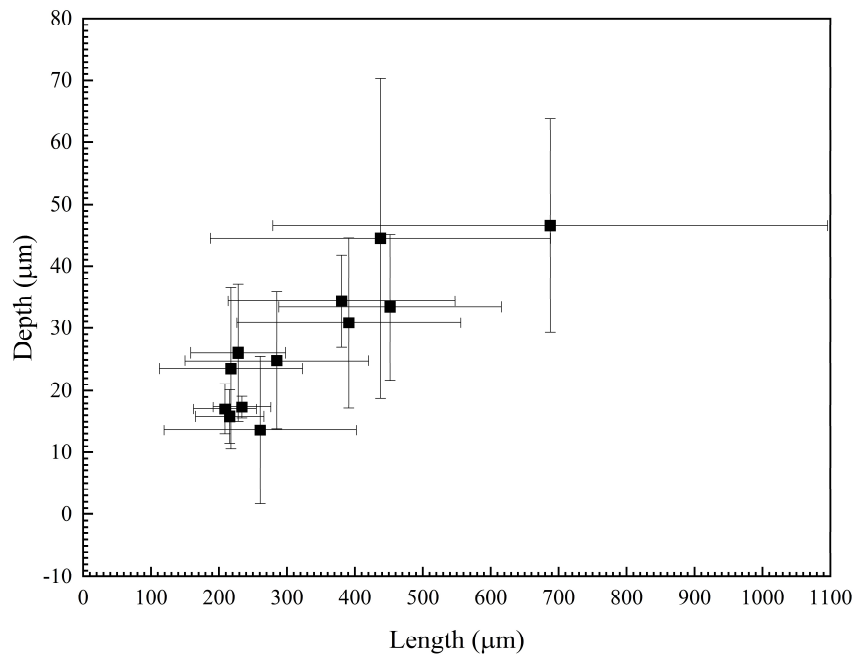
Figure 17 – Relationship between the length of the observed cracks and their depth.

The length and depth showed little variation or trend. It can only be clearly observed that the higher the load, the greater the length and depth. Apparently, there is a greater tendency for crack length on the side B for the 1500 MPa - lower tests and a propensity for shorter crack length on the same side for the 1500 MPa - upper tests. Although only two repetitions were performed for each parameter of a test that was never performed, more tests should be performed to analyse if there is a real trend or if this finding results from a natural distribution of results.

Nevertheless, it would be better to perform more tests to be more confident of this trend because only two repetition tests were performed. It is also possible that the crack-like defects may have broken off during the test, and their length/depth is statistically altered. Only a large amount of testing can guarantee certainty between a more significant trend in crack length and crack depth.

The hardness profile relationship showed a maximum hardness near the surface reached plateaus between 900 HV and 1000 HV. This hardness feature, although somewhat higher, agrees with Pereira *et al.* [30]. It was observed that spheroidized cementite microstructure has considerable potential work-hardening.

And lastly, Figure 16 reveals a distinct peak in average hardness near the surface, followed by a significant decline as one moves away. Beyond the fissure, there is a moderate subsequent increase, diminishing as it extends from the surface. Considering the initial composition of the inner surface of the crack as part of the disc's surface, a substantial

decrease in hardness is evident compared to the fresh surface. This is attributed to reduced surface deformation on the old surface, no longer exposed to the same conditions as the newly deformed region. Moreover, the heat generated during the rolling/sliding wear test contributes to stress relief and recovery phenomena, resulting in a surface less hardened than the original microstructure but harder than the adjacent region.

6. Conclusions

This study performed a new twin-disc test using a disc with all the microstructures present in the flash-butt-welded rail HAZ. Thus, it was possible to conclude that:

- There was microstructural heterogeneity along the disc, with different local mechanical properties and providing some distinct characteristics. The main characteristics was the substantial deformation in the softer regions creating valleys in the four spheroidization regions at the HAZ boundary.
- The mass loss of the driven disc was lower than that of the driving disc.
- Macro-sized cracking (termed master cracks) or RCF crack concentrations were observed in the central regions and at the HAZ boundary. These master cracks/ crack clusters coincide exactly after the strain valleys observed by the localized deformation of the disc and with the central region of the weld, i.e., exactly in the regions with softer microstructure (spheroidized cementite and pro-eutectoid ferrite).
- Spheroidized microstructure was observed in the upper region of the master cracks. The decrease in surface roughness and the valleys formed in the regions just before the cracks suggest that these larger cracks were formed by deformation (extrusion). An oxide layer was observed on the bottom surface of one master crack, supporting the extrusion hypothesis.
- The deleterious effect of the presence of pro-eutectoid ferrite on RCF crack propagation was confirmed. In the central region, meta-cluster cracks were observed, and in the cross-section metallography, the crack tip coincided with the region with deformed pro-eutectoid ferrite.

References

[1]   R. Ordóñez Olivares, C.I. Garcia, A. DeArdo, S. Kalay, F.C. Robles Hernández, Advanced metallurgical alloy design and thermomechanical processing for rails steels for North American heavy haul use, Wear. 271 (2011) 364–373. https://doi.org/10.1016/j.wear.2010.10.048.

[2]   R. Roberti, G. Donzella, M. Faccoli, A. Ghidini, A. Mazz, A. Mazzù, R. Roberti, The competitive role of wear and RCF in a rail steel, Eng. Fract. Mech. 72 (2005) 287–308. https://doi.org/10.1016/j.engfracmech.2004.04.011.

[3]   International Heavy Haul Association (IHHA), Guidelines to Best Practices for Heavy Haul Railway Operation: Wheel and Rail Interface Issues, First Edit, Virginia Beach, 2001.

[4]   I.M. Hutchings, Tribology: Friction and wear of engineering materials, Butterworth Heinemann, Cambridge, 2017.

[5]   L. Singh, Rolling Contact Fatigue in Rails – an Overview, IPWE Semin. (2011).

[6]   J. Lundmark, Rail Grinding and its impact on the wear of Wheels and Rails, Luleå University of Technology, 2007.

[7]   H. Mansouri, A. Monshi, Microstructure and residual stress variations in weld zone of flash-butt welded railroads, Sci. Technol. Weld. Join. 9 (2004) 237–245. https://doi.org/10.1179/136217104225012201.

[8]   R.R. Porcaro, D.A.P. de Lima, G.L. de Faria, L.B. Godefroid, L.C. Cândido, Microestrutura e propriedades mecânicas de um aço para trilhos ferroviários soldado por centelhamento, Soldag. Inspeção. 22 (2017) 59–71.

[9]   R.R. Porcaro, G.L. Faria, L.B. Godefroid, G.R. Apolonio, L.C. Cândido, E.S. Pinto, Microstructure and mechanical properties of a flash butt welded pearlitic rail, J. Mater. Process. Technol. 270 (2019) 20–27. https://doi.org/10.1016/j.jmatprotec.2019.02.013.

[10]   L.F. Bauri, L.H.D. Alves, H.B. Pereira, A.P. Tschiptschin, H. Goldenstein, The role of welding parameters on the control of the microstructure and mechanical properties of rails welded using FBW, J. Mater. Res. Technol. 9 (2020) 8058–8073.

https://doi.org/10.1016/j.jmrt.2020.05.030.

[11]   L.F. Bauri, Soldagem de topo com centelhamento de trilhos ferroviários: caracterização estrutural, propriedades mecânicas e desgaste, Universidade de São Paulo, 2019.

[12]   H.L. Ito, J.D.C. Gomes, Análise de falhas - um dever do IPT, Rev. IPT Tecnol. e Inovação. 3 (2019) 35–64.

[13]   L.B. Godefroid, G.L. Faria, L.C. Cândido, T.G. Viana, Fatigue Failure of a Flash Butt Welded Rail, Procedia Mater. Sci. 3 (2014) 1896–1901. https://doi.org/10.1016/j.mspro.2014.06.306.

[14]   H. Farhangi, S.M. Mousavizadeh, Horizontal split-web fractures of flash butt welded rails, Proc. 8th Int. Fract. Conf. (2007) 509–517.

[15]   A. Enshaeian, P. Rizzo, Stability of continuous welded rails: A state-of-the-art review of structural modeling and nondestructive evaluation, J. Rail Rapid Transit. 235 (2021) 1291–1311. https://doi.org/10.1177/0954409720986661.

[16]   N.A. Kozyrev, A.A. Usoltsev, R.E. Kryukov, R.A. Shevchenko, R.A. Gizatulin, A. V. Valueva, Modern methods of rail welding, Key Eng. Mater. 736 KEM (2017) 116–121. https://doi.org/10.4028/www.scientific.net/KEM.736.116.

[17]   K. Saita, K. Karimine, M. Ueda, Trends in Rail Welding Technologies and Our Future Approach, Nippon Steel Sumitomo Met. Tech. Rep. (2013) 84–92.

[18]   M. Gupta, S. Bisht, Technology and Trends in Flash Butt Welding, CORE, 2016-Conf. Railw. Excel. (2016).

[19]   A. Joerg, B. Eisenkolb, J. Goriupp, A. Zlatnik, R. Hochfellner, S. Scheriau, H.P. Brantner, Hyper-Eutectoid Rail Steels – Best in Class And Still to be Further Develope, IHHA. (2015).

[20]   L.H.D. Alves, M.L. Lagares, R.M.M. Filho, T. Tepedino, H. Goldenstein, Predictive Mathematical Modeling of the Flash-Butt Welding Process to Optimize the Properties of Welds of Premium and Super Premium Rails, Int. Heavy Haul Assoc. (2019).

[21]   H.B. Pereira, E. Anderson, A. Echeverri, L. Henrique, D. Alves, H. Goldenstein, Evaluation of the Effect of Heat Input and Cooling Rate of Rail Flash-Butt Welding using Finite Element Method Simulation, Soldag. Inspeção. 27 (2022) 1–18. https://doi.org/https://doi.org/10.1590/0104-9224/SI27.01.

[22] K. Saita, M. Ueda, T. Miyazaki, Developing technologies to improve the reliability of flash-butt welds, 11th Int. Heavy Haul Assoc. Conf. (2017) 208–215.

[23] L.P. Nishikawa, H. Goldenstein, Divorced Eutectoid on Heat-Affected Zone of Welded Pearlitic Rails, J. Miner. Met. Mater. Soc. (2018). https://doi.org/10.1007/s11837-018-3213-5.

[24] J.D. Verhoeven, E.D. Gibson, The divorced eutectoid transformation in steel, Metall. Mater. Trans. A. 29 (1998) 1181–1189.

[25] K. Ankit, R. Mukherjee, B. Nestler, Deviations from cooperative growth mode during eutectoid transformation: Mechanisms of polycrystalline eutectoid evolution in Fe-C steels, Acta Mater. 97 (2015) 316–324. https://doi.org/10.1016/j.actamat.2015.06.050.

[26] H.B. Pereira, E.A. Ariza Echeverri, D.M.A. Centeno, S. da S. de Souza, L.F. Bauri, M.D. Manfrinato, M. Masoumi, L.H.D. Alves, H. Goldenstein, Effect of pearlitic and bainitic initial microstructure on cementite spheroidization in rail steels, J. Mater. Res. Technol. 23 (2023) 1903–1918. https://doi.org/10.1016/j.jmrt.2023.01.087.

[27] A.B. Rezende, S.T. Fonseca, F.M. Fernandes, R.S. Miranda, F.A.F. Grijalba, P.F.S. Farina, P.R. Mei, Wear behavior of bainitic and pearlitic microstructures from microalloyed railway wheel steel, Wear. 456–457 (2020) 203377. https://doi.org/10.1016/j.wear.2020.203377.

[28] J.P. Liu, Y.Q. Li, Q.Y. Zhou, Y.H. Zhang, Y. Hu, L.B. Shi, W.J. Wang, F.S. Liu, S.B. Zhou, C.H. Tian, New insight into the dry rolling-sliding wear mechanism of carbide-free bainitic and pearlitic steel, Wear. 432–433 (2019). https://doi.org/10.1016/j.wear.2019.202943.

[29] K.M. Lee, A.A. Polycarpou, Wear of conventional pearlitic and improved bainitic rail steels, Wear. 259 (2005) 391–399. https://doi.org/10.1016/j.wear.2005.02.058.

[30] H.B. Pereira, L.H. Alves, A.B. Rezende, P.R. Mei, H. Goldenstein, Influence of the microstructure on the rolling contact fatigue of rail steel: Spheroidized pearlite and fully pearlitic microstructure analysis, Wear. 499 (2022) 204299. https://doi.org/10.1016/j.wear.2022.204299.

[31] P. Mutton, J. Cookson, C. Qiu, D. Welsby, Microstructural characterisation of rolling contact fatigue damage in flashbutt welds, Wear. 366–367 (2016) 368–377. https://doi.org/10.1016/j.wear.2016.03.020.

[32] L.H.D. Alves, R. Malheiros, R. Souza, A. Sinatora, H. Goldenstein, Mathematical Modeling to Predict and Optimize Mechanical Properties and Microstructural Heterogeneities of Welds and Heat- Affected Zones in Thermite Welding Process, Int. Heavy Haul Assoc. (2019).

[33] B.L. Bramfitt, F.B. Fletcher, J.A. Davis Jr, Method of making a hypereutectoid, head-hardened steel rail, (2012).

[34] D.I. Fletcher, J.H. Beynon, Development of a Machine for Closely Controlled Rolling Contact Fatigue and Wear Testing, J. Test. Eval. 28 (2000) 267–275. https://doi.org/10.1520/jte12104j.

[35] S. Timoshenko, J.N. Goodier, Theory of elasticity, in: McGraw Hill, 1951: pp. 366–382.

[36] U.P. Singh, R. Singh, Wear investigation of wheel and rail steels under conditions of sliding and rolling-sliding contact with particular regard to microstructural parameters, Wear. 170 (1993) 93–99. https://doi.org/10.1016/0043-1648(93)90355-P.

[37] D.I. Fletcher, J.H. Beynon, Equilibrium of crack growth and wear rates during unlubricated rolling-sliding contact of pearlitic rail steel, Proc. Inst. Mech. Eng. Part F J. Rail Rapid Transit. 214 (2000) 93–105. https://doi.org/10.1243/0954409001531360.

[38] J. Seo, S. Kwon, D. Lee, H. Choi, Analysis of contact fatigue crack growth using twin-disc tests and numerical evaluations, Int. J. Fatigue. 55 (2013) 54–63. https://doi.org/10.1016/j.ijfatigue.2013.05.005.

[39] J.W. Seo, H.K. Jun, S.J. Kwon, D.H. Lee, Rolling contact fatigue and wear of two different rail steels under rolling-sliding contact, Int. J. Fatigue. 83 (2016) 184–194. https://doi.org/10.1016/j.ijfatigue.2015.10.012.

[40] Q. Li, C. Zhang, H. Chen, Chen, Z. Yang, Microstructural Evolution of a Hypoeutectoid Pearlite Steel under Rolling-sliding Contact Loading, J. Iron Steel Res. Int. 23 (2016) 1054–1060. https://doi.org/10.1016/S1006-706X(16)30157-1.

[41] A.J. Perez-Unzueta, J.H. Beynon, Microstructure and wear resistance of pearlitic rail steels, Wear. 164 (1993) 173–182.

[42] American Society for Testing and Materials, ASTM E92: Standard Test Method for Microindentation Hardness of Materials, ASTM Int. (2017).

https://doi.org/10.1520/E0384-17.

[43] Association Of American Railroad, AAR M-107/M-208: Manual of Standards and Recommended Practices Wheels and Axles, (2011).

[44] J.V. de O. Cordeiro, Program_image, (2023). https://github.com/Joao-Vtr/Program_image/blob/fdf7e054bd1765e152908acc826112e0b2c3d796/Program.txt.

[45] G. Krauss, Steels : Processing, Structure, and Performance, ASM International, 2015. https://doi.org/10.1007/s007690000247.

[46] ASM Handbook, Properties and Selection: Irons, Steels, and High-Performance Alloys, ASM International, Material Park, 1995.

[47] Y. Hu, W.J. Wang, M. Watson, K. Six, H. Al-maliki, A. Meierhofer, R. Lewis, Wear of driving versus driven discs in a twin disc rolling-sliding test, Wear. 513 (2023). https://doi.org/10.1016/j.wear.2022.204528.

[48] H.H. Ding, C.G. He, L. Ma, J. Guo, Q.Y. Liu, W.J. Wang, Wear mapping and transitions in wheel and rail materials under different contact pressure and sliding velocity conditions, Wear. 352–353 (2016) 1–8. https://doi.org/10.1016/j.wear.2016.01.017.

[49] N. Tassini, X. Quost, R. Lewis, R. Dwyer-joyce, C. Ariaudo, N. Kuka, A numerical model of twin disc test arrangement for the evaluation of railway wheel wear prediction methods, Wear. 268 (2010) 660–667. https://doi.org/10.1016/j.wear.2009.11.003.

[50] R. Lewis, R.S. Dwyer-Joyce, Wear mechanisms and transitions in railway wheel steels, Proc. Inst. Mech. Eng. Part J J. Eng. Tribol. 218 (2004) 467–478.

[51] T.G. Pearce, N.D. Sherratt, Prediction of wheel profile wear, Wear. 144 (1991) 343–351.

[52] M. Steenbergen, R. Dollevoet, On the mechanism of squat formation on train rails - Part II: Growth, Int. J. Fatigue. 47 (2013) 373–381. https://doi.org/10.1016/j.ijfatigue.2012.04.019.

[53] J.E. Garnham, C.L. Davis, Very early stage rolling contact fatigue crack growth in pearlitic rail steels, Wear. 271 (2011) 100–112. https://doi.org/10.1016/j.wear.2010.10.004.

[54] K. Cvetkovski, J. Ahlström, M. Norell, C. Persson, Analysis of wear debris in rolling contact fatigue cracks of pearlitic railway wheels, Wear. 314 (2014) 51–56. https://doi.org/10.1016/j.wear.2013.11.049.

[55] American Society for Testing and Materials, ASTM E1823: Relating to Fatigue and Fracture Testing, (2013). https://doi.org/10.1520/E1823-13.2.

[56] A. Kapoor, Wear by plastic ratchetting, Wear. 212 (1997) 119–130. https://doi.org/10.1016/S0043-1648(97)00083-5.

[57] F.J. Franklin, T. Chung, A. Kapoor, Ratcheting and fatigue-led wear in rail – wheel contact, 26 (2003) 949–955. https://doi.org/10.1046/j.1460-2695.2003.00703.x.

[58] T.L. Anderson, Fracture Mechanics: Fundamentals and Applications, Taylor & Francis Group, Boca Raton, 2005.

[59] UIC Code - 712, Handbook of Rail Defects, International Union of Railways, 2002.

[60] M. Mesaritis, M. Shamsa, P. Cuervo, J.F. Santa, A. Toro, M.B. Marshall, R. Lewis, A laboratory demonstration of rail grinding and analysis of running roughness and wear, Wear. 456–457 (2020) 203379. https://doi.org/10.1016/j.wear.2020.203379.